Impact of Backbone Composition on Homopolymer Dynamics and Brush Block Copolymer Self-Assembly

Journal:	*Polymer Chemistry*
Manuscript ID	PY-ART-07-2020-001007.R1
Article Type:	Paper
Date Submitted by the Author:	16-Sep-2020
Complete List of Authors:	Boyle, Bret; Colorado State University, Chemisry Collins, Joeseph; Colorado State University, Chemisry Mensch, Tara; Colorado State University, Chemisry Ryan, Matthew; Colorado State University, Chemisry Newell, Brian; Colorado State University, Chemistry Department Miyake, Garret; Colorado State University, Chemisry; Colorado State University

Impact of Backbone Composition on Homopolymer Dynamics and Brush Block Copolymer Self-Assembly

Bret M. Boyle,[a] Joseph L. Collins,[a] Tara E. Mensch,[a] Matthew D. Ryan,[a] Brian S. Newell,[a] and Garret M. Miyake[a*]

[a]Department of Chemistry,
Colorado State University, Fort Collins, Colorado
*Corresponding Authors: Garret.Miyake@colostate.edu

ABSTRACT

Four series of brush block copolymers (BBCP), with near identical side chain compositions but varying backbone structures, were synthesized to investigate the effect of backbone structure on the process of thermal BBCP self-assembly to photonic crystals (PCs). Each of the self-assembled PC films were examined by reflection measurements, small angle X-ray scattering measurements, and scanning electron microscopy to compare the resulting properties of the polymeric photonic crystal and the nanostructured morphology impacted by the backbone structure. It was found that the composition of the brush backbone within a BBCP has a dramatic effect on the ability of the BBCP to self-assemble into ordered nanostructures and on the local ordering of the nanostructure morphology accessed with higher molecular weight (MW) BBCPs (> 1,500 kg/mol). BBCPs with a norbornene imide-based backbone were able to thermally self-assemble to longer wavelength reflecting PCs and had higher fidelity ordering of lamellar nanostructures with higher MW polymers. By analyzing the melt rheological responses of the backbone compositions, both as linear polymers and homobrush polymers, it was concluded that the inherent fragility of the backbone promotes enhanced local ordering in the lamellar nanostructure morphology as well as access to larger domain sizes.

INTRODUCTION

Photonic crystals (PC) are periodic dielectric materials possessing a photonic band gap that inhibits the propagation of specific frequencies of light.[1,2] The wavelength of reflected light by the PC is dictated by the interaction of light with the nanostructured morphology and enables applications as light guides, optical filters, and reflective coatings.[3,4,5] There are many routes to synthetic PCs, but an attractive economical and scalable method to form PCs is through the self-assembly of block copolymers (BCP) to nanostructured materials.[6,7,8,9,10,11] Block copolymers can be constructed from diverse polymer architectures such as linear,[12] dendritic,[6,13] or bottlebrush copolymers.[14,15] The self-assembly of linear BCPs (LBCP) is largely governed by the interaction parameter of the two blocks, the volume fraction of each block, and the degree of polymerization of each block.[16,17] However, the inherent chain entanglement in linear polymers challenges the ability of LBCPs to self-assemble to domain sizes large enough to reflect wavelengths of light longer than green.[18] Therefore, by exploiting more rigid polymer architectures, polymeric PC materials can be enabled to reflect wavelengths of light across the visible spectrum and into the near-IR, in part due to a reduction in the amount of polymer chain entanglement.[6,13,19,20,21] In particular, bottlebrush BCPs (BBCP) significantly reduce chain entanglement and have been shown to rapidly self-assemble to domains large enough to reflect wavelengths of light across the visible spectrum and into the near-IR.[22,23,24,25,26,27,28]

The bottlebrush polymer architecture consists of densely spaced polymeric side chains grafted onto a central polymer backbone.[29] The polymeric side chains promote the cylindrical conformation of bottlebrush macromolecules due to the steric repulsion between neighboring side chains. This cylindrical conformation significantly influences bulk materials properties, such as extending the persistence length, reducing the entanglement modulus, and creating a secondary relaxation.[30,31,32,33,34,35] The bottlebrush backbone composition plays an essential role in the global conformation of the homobrush polymers, both due to the phenomena of excluded volume between the side chains and the inherent fragility of the polymer.[36,37,38,39] Synthetic advancements allow alteration of the side chains or the main chain backbone to modulate the properties of the brush polymer and the resulting brush polymer bulk material. [40]

Currently, however, there is a lack of insight into how the dynamics of a homobrush polymer translate to a BBCP's dynamics. Among the various synthetic schemes, there are no established advantages of one synthetic route to a bottlebrush polymer over another with respect to synthesizing a BBCP that can efficiently self-assemble to a PC capable of efficiently reflecting wavelengths of light across the visible spectrum. [41,42] There are reported advantages to choosing a macromonomer (MM) anchor group for ROMP that will promote high MM conversion and high MW brushes, [43] however, the effect of these anchor groups on the melt dynamics of self-assembly of the resulting BBCPs are not currently known. Watkins and co-workers have made insightful observations into how the backbone length, side chain length, molecular asymmetry, and volume fraction of BBCPs affect the nanostructure phase map and the relaxation modes of BBCPs.[44,45] Unfortunately, there is no clear predictor of how modifying the backbone structure of the BBCP influences the process of self-assembly and the resulting PC properties. The impact of the backbone on self-assembly and the resulting PC properties is of high importance, especially when considering the myriad of synthetic routes available to BBCPs. The composition of the backbone and influences on the BBCP could inform whether a certain synthetic route to BBCPs would be preferable to target macromolecular properties for a specific application.

Herein, we report the effect of varying backbone structure on BBCP self-assembly and the resulting properties of the BBCP PC. We couple our observations of the BBCP self-assembly and PC film properties with an investigation into the polymer dynamics of linear and brush homopolymers containing identical backbone compositions to those of the BBCPs. The results reveal that the backbone composition of a BBCP imparts a significant influence on the reflection and lamellar nanostructured morphology of the resulting PC material. Overall, it is observed that more fragile polymer backbones result in more efficient domain interface relaxation and manifest into encouraging higher MW BBCPs to self-assemble to longer wavelength reflecting PCs.

RESULTS AND DISCUSSION

To investigate the effect of backbone composition on the self-assembly of BBCPs to visible light reflecting, polymeric PCs, four different series of varying molecular weight (MW) BBCPs were synthesized using ruthenium-mediated ring opening metathesis polymerization (ROMP) (Scheme 1). The macromonomers used in this study consisted of two different poly(*racemic*-lactide) (PLA) macromonomers (index of refraction is approximately 1.49), containing either a norbornene (NB-PLA, $M_n \sim 3,300$ g/mol) or a norbornene imide (NBI-PLA, $M_n \sim 3,400$ g/mol) chain end, as well as two poly(styrene) (PS) macromonomers (index of refraction is approximately 1.59), possessing either a norbornene (NB-PS, $M_n \sim 3,600$ g/mol) or a norbornene imide (NBI-

PS, M_n ~ 4,400 g/mol) chain end. The resulting BBCP series, denoted by *p*(NBI-PLA)-*b*-*p*(NBI-PS), *p*(NB-PLA)-*b*-*p*(NBI-PS), *p*(NBI-PLA)-*b*-*p*(NB-PS), or *p*(NB-PLA)-*b*-*p*(NB-PS), were isolated as colorless materials before being self-assembled by thermal annealing for 16 hours under vacuum at a temperature of 140 °C. This annealing temperature was chosen because it is at least 40 °C above the glass transition temperature (T_g) of any of the brush block's T_g values (Figures S89-S95), which enables self-assembly. To prepare the samples by thermal annealing, each polymer sample was placed between two glass microscope slides (the glass slides were cleaned with acetone before use) with two paper clips compressing the sample between the slides. These samples were then placed in a vacuum oven at 140 °C. Equal molar ratios of the macromonomers were polymerized to target a consistent BBCP composition of 60-70 % poly(styrene) content to 30-40 % poly(lactide) content (Table S15) and a lamellar nanostructure due to the ease of observing a change in the wavelength of reflection with a change in the domain size with increasing BBCP MW using a modified form of Bragg's Law (Scheme 1).[46]

Scheme 1. Synthetic approach to the four distinct BBCPs and their self-assembly to polymeric photonic crystals.

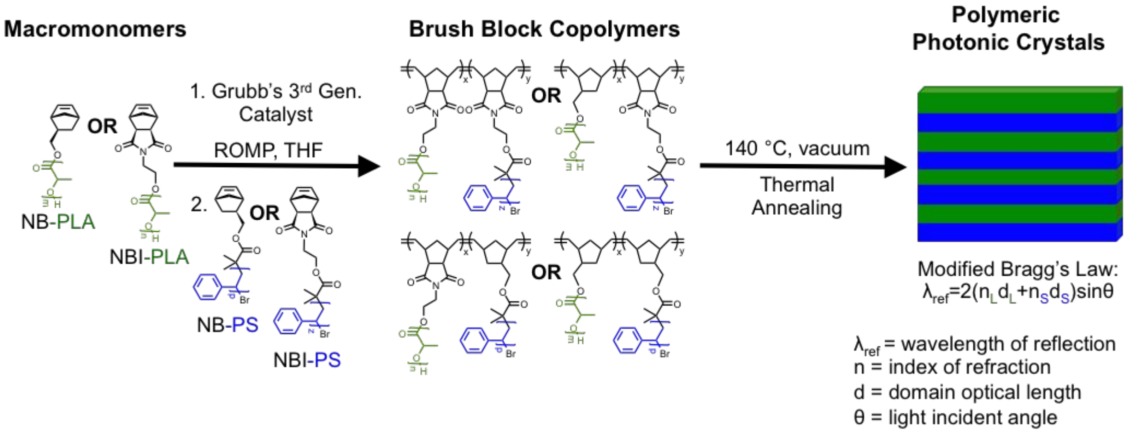

After thermal annealing, the films reflected wavelengths of light in the ultraviolet or visible spectrum due to the periodicity of the assembled nanostructure. The reflection profile of each of the four series of self-assembled BBCP films was characterized directly by measuring the percent of incident wavelengths of light across the ultraviolet and visible spectrum reflected by the assembled film (Figure 1A-D). These measurements were performed using a UV-Vis spectrophotometer outfitted with a diffuse reflectance accessory (DRA). The films studied were prepared between two glass slides fastened together by a paper clip on either side of the slide. Hence, the intensity of reflection traces (Figure 1A-D) should not be considered to be representative of the film as the glass slides are causing interference, which further restricts quantifying the number of lamellar layers throughout the film.

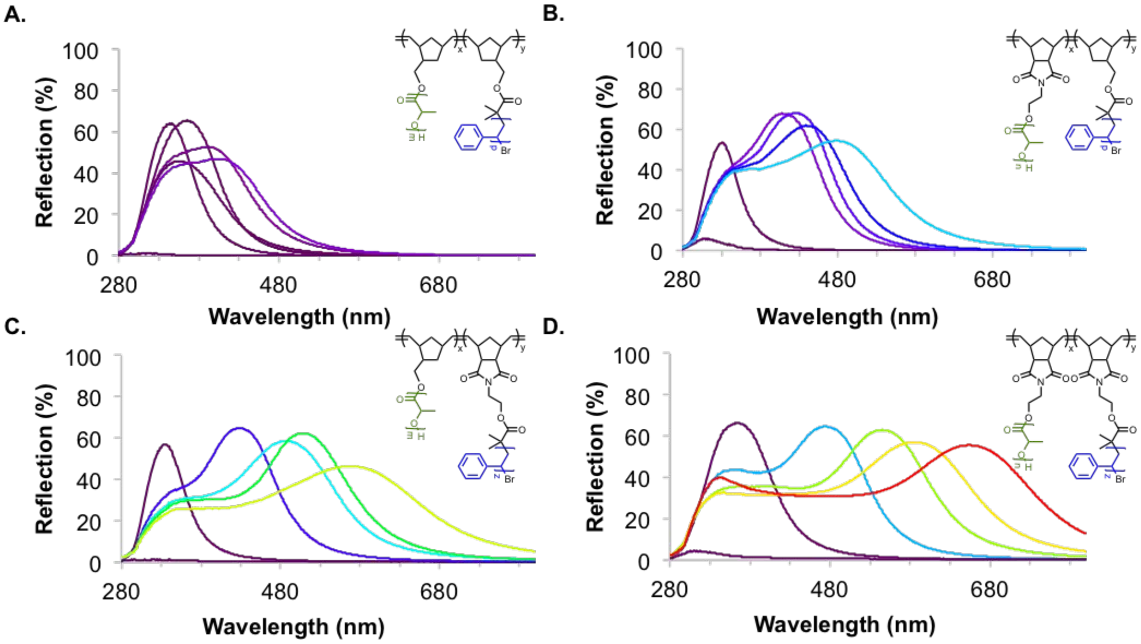

Figure 1. Plots of of reflection (%) vs. wavelength (nm) for each of the four BBCP MW series assembled films (*p*(NB-PLA)-*b*-*p*(NB-PS) (A), *p*(NBI-PLA)-*b*-*p*(NB-PS) (B), *p*(NB-PLA)-*b*-*p*(NBI-PS) (C), and *p*(NBI-PLA)-*b*-*p*(NBI-PS) (D)).

Interestingly, although studying similar MW ranges and dispersity values (< 1.3; See Tables S11-S14) of polymers, each of the series of BBCP annealed films reflection profiles spanning different ranges of wavelengths. The majority of the weight fraction of each of these BBCP compositions is almost indistinguishable, with the polymeric side chains being extremely similar, if not identical. The only significant compositional difference between each of these four BBCP series is the identity of the backbone. Even with higher MW BBCPs, the annealed films from the *p*(NB-PLA)-*b*-*p*(NB-PS) series did not reflect wavelengths of light longer than violet (406 nm), while the films fabricated from *p*(NBI-PLA)-*b*-*p*(NBI-PS) reflect wavelengths of light across the UV-visible spectrum ranging from ultraviolet (300 nm) to red-orange (655 nm).

To conceptualize these different wavelengths of reflection for each BBCP composition, it helps to visualize how the brush macromolecule arranges itself within the nanostructure morphology (Figure 2A) and how that might affect a modified Bragg's law. Each of the domains throughout all of the assembled films contain the same respective indices of refraction (n_L and n_S), therefore, the difference must stem from differences in the domain sizes of each ordered domain (d_L and d_S). It is often thought that the domain sizes of each ordered domain are highly dependent on the MW of each polymer within each domain; therefore, the higher MW of a polymer, the greater the domain size, and the greater the wavelength of reflection is of the resulting photonic crystal. To further investigate the differences in morphology that arises from each of these four BBCP compositions, Figure 2B plots the maximum wavelength of reflection with respect to each polymer's number-average MW (M_n). The resulting relationship between the maximum wavelength of reflection and the polymer's M_n highlights the impact that the different backbone compositions have on the reflection of each of the BBCP series. The slope (k) of each of the best-fit lines in Figure 2B provides a means to quantify how increasing MW, or a higher degree of polymerization (DP), will affect the maximum wavelength of reflection of the thermally annealed films for each series. The *p*(NBI-PLA)-*b*-*p*(NBI-PS) film series resulted in a k = 0.31, meaning that this backbone composition allows for a 0.31 nm increase in wavelength of reflection for every kilogram per mole of BBCP that is added to the polymeric PC film. In contrast, the k of the *p*(NB-PLA)-*b*-*p*(NB-PS) series is 0.04, which implies that an approximately eightfold increase in BBCP MW of this composition is needed to have domain sizes large enough to reflect similar wavelengths as the *p*(NBI-PLA)-*b*-*p*(NBI-PS) film composition does. Comparatively, by replacing the NB-PS block with a NBI-PS block in the *p*(NB-PLA)-*b*-*p*(NB-PS) composition, the k value increases to 0.16, rather than only increasing to 0.08, as replacing the NB-PLA block with a NBI-PLA block in the *p*(NB-PLA)-*b*-*p*(NB-PS) composition does.

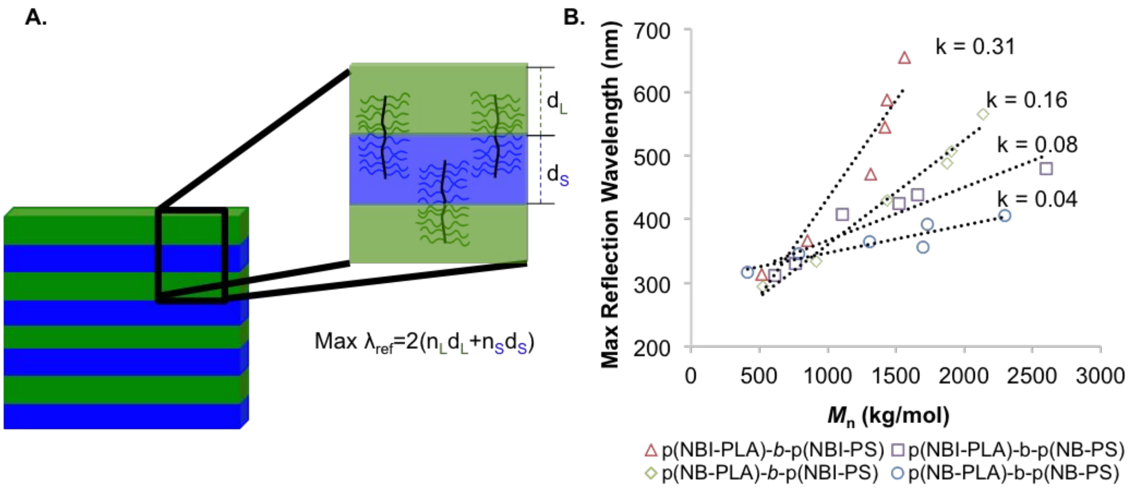

Figure 2. A conceptual schematic of the nanostructure morphology observed and how the brush polymers would align within the morphology to determine the domain spacing (d_L and d_S) (A). A plot of the max wavelength of reflection for each assembled film within each of the four BBCP series vs. the M_n of each polymer (k = slope of best fit line) (B).

Although the *p*(NBI-PLA)-*b*-*p*(NBI-PS) films are able to reflect wavelengths of light across the visible spectrum and have the greatest m value, the bandwidths of the PCs are large and broaden with increasing maximum wavelengths of reflection. The bandwith of a PC determines which range of wavelengths of light are reflected, and the ability to modulate the PC bandwith allows for engineering PCs for specific applications.13 For certain applications a broad bandwith may be desirable over a narrow bandwith. The bandwith of a PC is related to the global ordering of the nanostructure morphology throughout the film by being a quantitative reflection of the uniformity of the ordering of the nanostructure morphology. For example, if a narrow bandwith is desired for an application, the global ordering of the nanostructure must be fairly uniform to restrict the interaction of the PC with only certain wavelengths of light within a small range. If a broad bandwith is needed, the global ordering of the nanostructure will not have a uniform global ordering to allow for many wavelengths of light to interact with the PC nanostructure. To measure the bandwith of a PC, the full-width-half-max (FWHM) value of the reflection trace was calculated. The lower measured FWHM value of 153 nm for the film assembled from the *p*(NB-PLA)-*b*-*p*(NB-PS) BBCP (2.30 x 10^3 kg/mol) implies that the global ordering of the lamellar nanostructure is significantly more uniform for the film assembled from the *p*(NBI-PLA)-*b*-*p*(NBI-PS) BBCP (1.56 x 10^3 kg/mol) with a FWHM of 428 nm (Table 1). In fact, the longer the maximum wavelength of reflection for each BBCP composition, or the greater the m value for each series, the less global ordering is present in the nanostructure. The backbone composition significantly affects the global ordering of the nanostructure of a BBCP PC film in addition to the maximum wavelength of reflection.

Table 1. FWHM values calculated for each of the BBCP PC films from the DRA reflection traces in Figure 1.

p(NB-PLA)-*b*-p(NB-PS)		**p(NBI-PLA)-*b*-p(NB-PS)**		**p(NB-PLA)-*b*-p(NBI-PS)**		**p(NBI-PLA)-*b*-p(NBI-PS)**	
M_n (kg/mol)	**FWHM (nm)**	**M_n (kg/mol)**	**FWHM (nm)**	**M_n (kg/mol)**	**FWHM (nm)**	**M_n (kg/mol)**	**FWHM (nm)**
4.14x10^2	63	6.13x10^2	50	5.24x10^2	91	5.20x10^2	62
7.87x10^2	65	7.66x10^2	48	9.18x10^2	55	8.50x10^2	91
1.31x10^3	89	1.11x10^3	135	1.44x10^3	143	1.31x10^3	210
1.73x10^3	134	1.52x10^3	149	1.88x10^3	214	1.42x10^3	280
1.70x10^3	101	1.66x10^3	174	1.90x10^3	138	1.43x10^3	344
2.30x10^3	153	2.60x10^3	235	2.13x10^3	334	1.56x10^3	428

To visualize the nanostructure morphology, SEM micrographs were collected for each of the thermally annealed films (Figures 3 and S56-S80). For the *p*(NB-PLA)-*b*-*p*(NB-PS) composition, as the BBCP MW increases, the local ordering of the lamellar nanostructure quickly deteriorates (Figure 3A, 3E, and 3I). For the *p*(NBI-PLA)-*b*-*p*(NB-

PS) composition (Figure 3B, 3F, and 3J), the local ordering of the nanostructure loses its fidelity with increasing MW. However, the *p*(NBI-PLA)-*b*-*p*(NB-PS) composition (1.11 x 10^3 kg/mol) does retain the ordering of its nanostructure morphology more effectively than that of the *p*(NB-PLA)-*b*-*p*(NB-PS) composition at intermediate MW (1.31 x 10^3 kg/mol). The more efficient ordering can be qualitatively demonstrated by a greater wavelength of reflection of 408 nm for the *p*(NBI-PLA)-*b*-*p*(NB-PS) composition (1.11 x 10^3 kg/mol) versus that of 365 nm for the *p*(NB-PLA)-*b*-*p*(NB-PS) composition (1.31 x 10^3 kg/mol). A similar trend exists moving from the *p*(NBI-PLA)-*b*-*p*(NB-PS) composition to the *p*(NB-PLA)-*b*-*p*(NBI-PS) composition (Figure 3C, 3G, and 3K). The highest MW sample of the *p*(NB-PLA)-*b*-*p*(NBI-PS) is more well-defined and ordered than that shown in the SEM micrograph of the highest MW of the *p*(NBI-PLA)-*b*-*p*(NB-PS) and reflects a longer wavelength of light. Lastly, the *p*(NBI-PLA)-*b*-*p*(NBI-PS) composition (Figure 3D, 3H, and 3L) maintains local ordering of the nanostructure throughout the entire MW series tested as seen by the reflecting the longest wavelength of reflection (Figures 1 and 2). Hence, the backbone composition of the BBCPs significantly impacts the local ordering of the thermally annealed film's nanostructure morphology. It is important to note that the nanostructure morphology observed in the SEM micrographs (Figure 3) does reflect a slightly asymmetric lamellar morphology, likely due to the slight asymmetry in the BBCP composition.

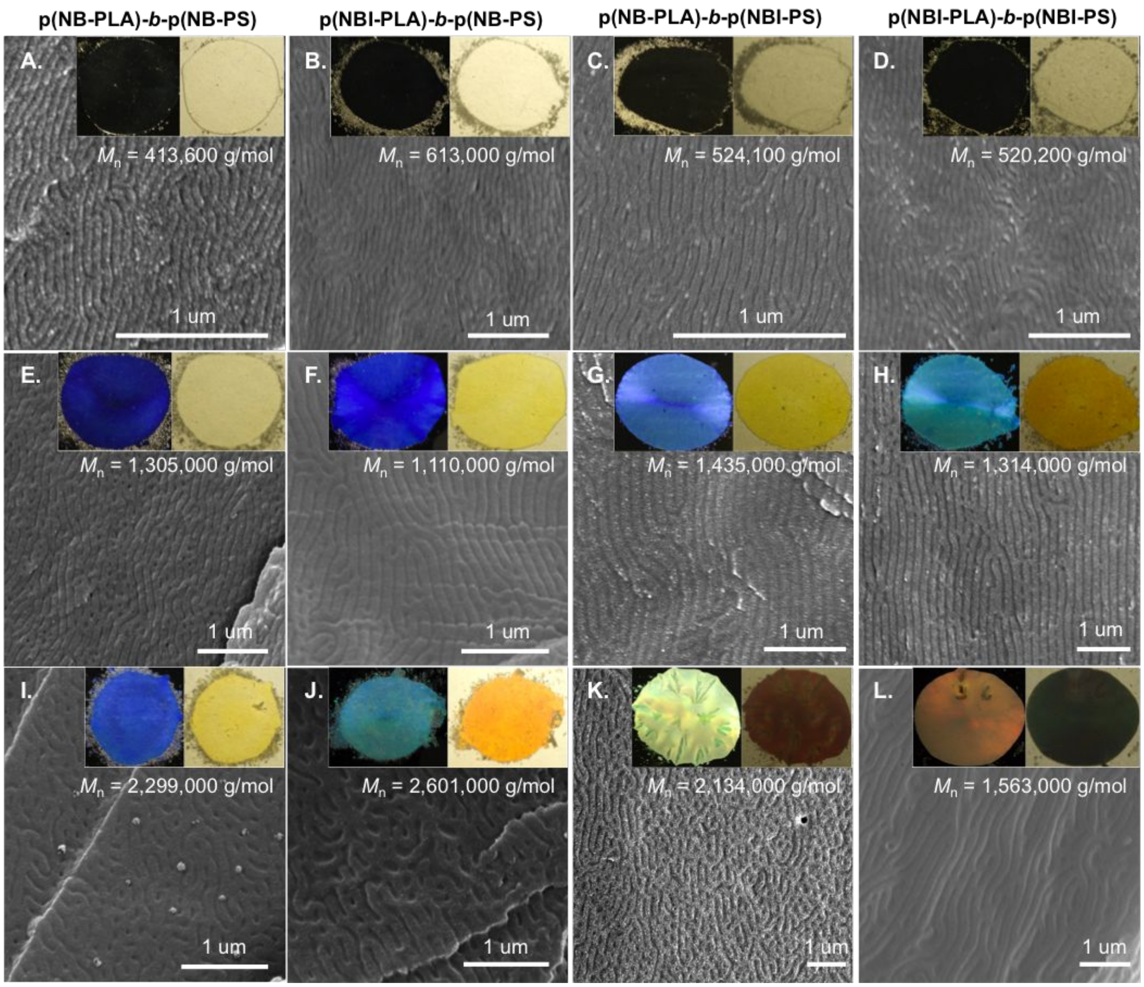

Figure 3. SEM micrographs of cross-sections of three films from each of the thermally annealed BBCP films of comparable MW (*p*(NB-PLA)-*b*-*p*(NB-PS) films shown in A, E, I; *p*(NBI-PLA)-*b*-*p*(NB-PS) films shown in B, F, J; *p*(NB-PLA)-*b*-*p*(NBI-PS) films shown in C, G, K; *p*(NBI-PLA)-*b*-*p*(NBI-PS) films shown in D, H, L) with photographs of the annealed film's (film area ≤ 3.14 cm^2) reflection (left inset picture) and transmission (right inset picture).

To confirm the lamellar nanostructure, Small-angle X-ray Scattering (SAXS) was used to describe the phase behavior of the four BBCPs with different backbone structures (Figure 4). The lowest MW BBCP samples of each of the four series (*p*(NB-PLA)-*b*-*p*(NB-PS) = 4.14 x 10^2 kg/mol, *p*(NBI-PLA)-*b*-*p*(NB-PS) = 6.13 x 10^2 kg/mol, *p*(NB-

PLA)-*b*-*p*(NBI-PS) = 5.24 x 10^2 kg/mol, *p*(NBI-PLA)-*b*-*p*(NBI-PS) = 5.20 x 10^2 kg/mol) were thermally annealed (140 °C, vacuum, overnight) in the bulk, and then cooled before collecting data. To collect data, the samples were first measured at room temperature (27 °C) before all of the samples were ramped to 140 °C in a period of six minutes. Once the samples reached 140 °C, the scattering of the assembled film was monitored over the next 72 minutes at six minute intervals before the temperature was ramped back to room temperature. Each of the four BBCP films exhibited evidence of the lamellar morphology (Figure 4). The lamellar domain spacings (d_{100}) (calculated from the primary peak q_{100} value from SAXS using the equation $d_{hkl} = 2\pi / q_{hkl}$) for each of the four films are within a comparable range from 63.3 nm to 89.2 nm (Table 2). Upon thermal annealing, the *p*(NB-PLA)-*b*-*p*(NBI-PS) sample (Figure 4C) and the *p*(NBI-PLA)-*b*-*p*(NBI-PS) sample (Figure 4D) do not show much structural change while the *p*(NB-PLA)-*b*-*p*(NB-PS) sample (Figure 4A) and the *p*(NBI-PLA)-*b*-*p*(NB-PS) sample (Figure 4B) both shift to lower q values over time. This observation might indicate swelling of these samples during the process of annealing. Further, *in-situ* SAXS experiments on non-annealed BBCPs of each series were completed to observe the temperature-dependence of the self-assembly of the BBCPs with different backbone structures (Figure S81). The morphology of each of the bulk, non-assembled BBCP samples was observed to form into the lamellar morphology during these *in-situ* SAXS experiments. After 72 minutes at 140 °C, each of these BBCP bulk samples were not as ordered as the films that were annealed overnight under vacuum and pressure (Figure 4), but the scattering patterns of each of the films still trend towards a lamellar morphology.

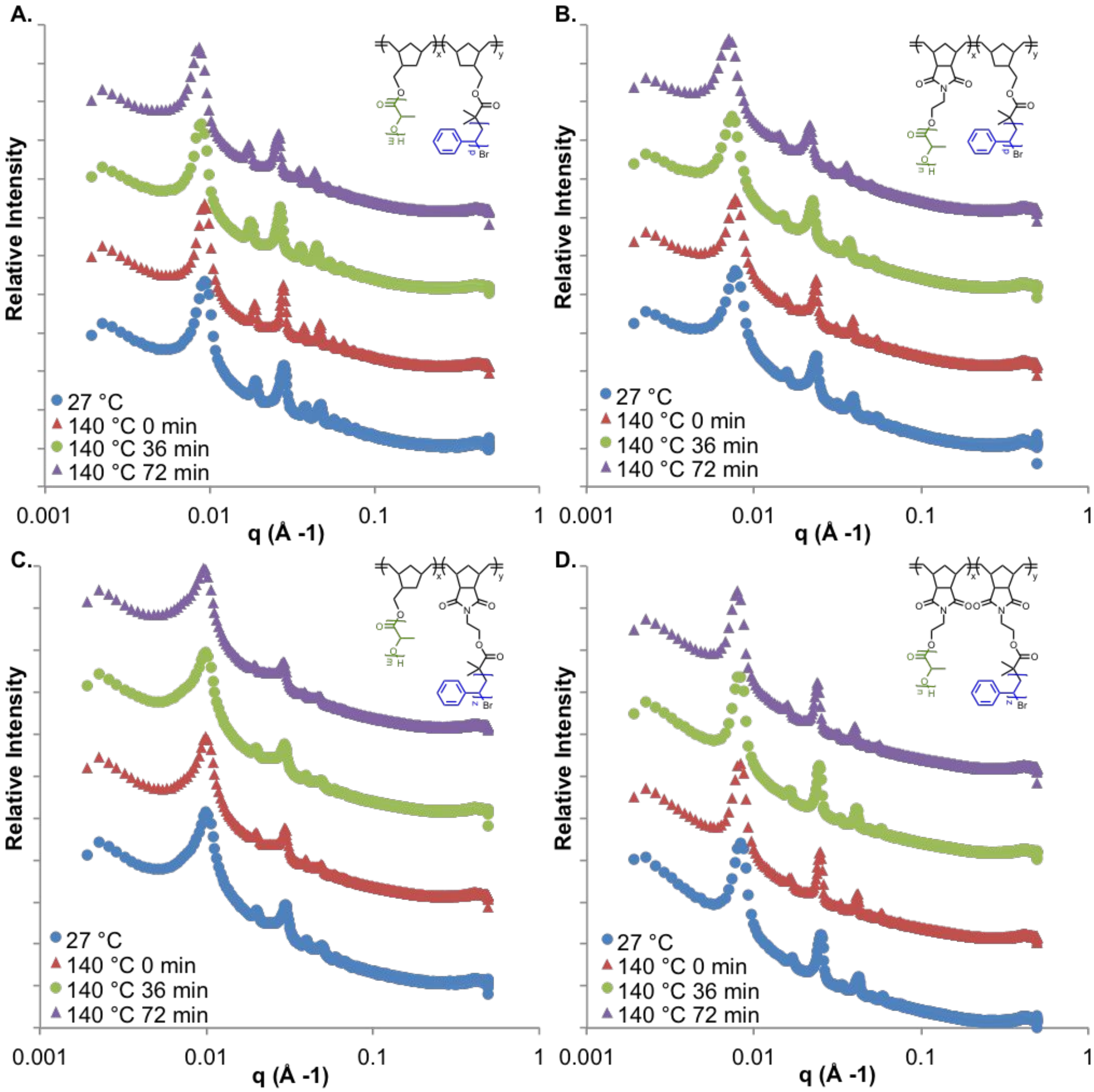

Figure 4. Log-log SAXS profiles for each of the four lowest MW BBCP assembled films (*p*(NB-PLA)-*b*-*p*(NB-PS) (A), *p*(NBI-PLA)-*b*-*p*(NB-PS) (B), *p*(NB-PLA)-*b*-*p*(NBI-PS) (C), and *p*(NBI-PLA)-*b*-*p*(NBI-PS) (D)). Spectra are vertically shifted for clarity.

Table 2. The primary scattering peak (q_{100}) values and domain spacing (d_{100}) values for each of the four polymers from SAXS experiments at 27 °C after annealing overnight at 140 °C. The estimated domain spacing values (d_{est}) from the SEM micrographs in Figure 3 are also included.

BBCP Sample	BBCP M_n (kg/mol)	q_{100} (Å^{-1})	d_{100} (nm)[a]	d_{est} (nm)[b]
p(NB-PLA)-*b*-p(NB-PS)	4.14×10^2	0.00864	72.7	83
p(NBI-PLA)-*b*-p(NB-PS)	6.13×10^2	0.00704	89.2	88
p(NB-PLA)-*b*-p(NBI-PS)	5.24×10^2	0.00993	63.3	70
p(NBI-PLA)-*b*-p(NBI-PS)	5.20×10^2	0.00801	78.5	90

[a] d_{100} values of microphase separated BBCPs were calculated using the equation $d_{hkl} = 2\pi / q_{hkl}$

[b] d_{est} values of microphase separated BBCPs were measurements estimated from the SEM micrographs in Figure 3

To gain insight into why the backbone composition affects the self-assembly processes of the BBCPs, MW series of linear and brush homopolymers were synthesized using ruthenium-mediated ROMP in an attempt to mimic the backbone composition and isolate the effect of each backbone component on each block of the BBCPs (Scheme 2). The polymer dynamics of these homopolymer series were characterized using rheological measurements.

Scheme 2. Synthetic strategy to homopolymers (linear and brush) with a norbornene backbone composition (A, Top to bottom: NB-Hep, NB-PLA, and NB-PS) and a norbornene imide backbone composition (B, Top to bottom: NBI-Dec, NBI-Hep, NBI-PLA, and NBI-PS).

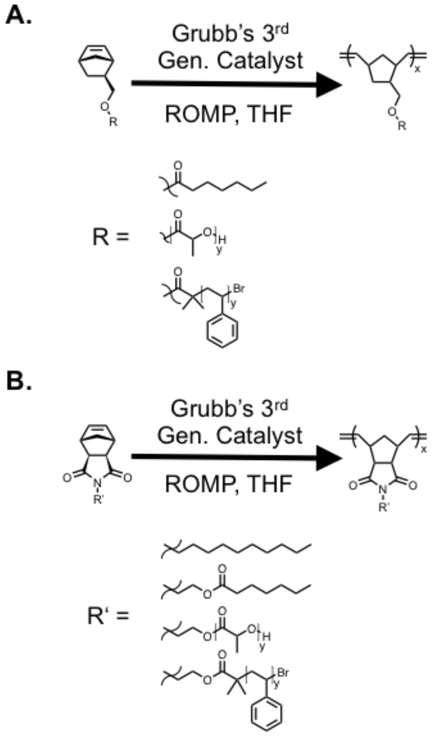

The three linear polymers were synthesized from monomers composed of a norbornene group functionalized with heptanoic acid (NB-Hep, Scheme 2A) or a norbornene imide group functionalized with either heptanoic acid (NBI-Hep, Scheme 2B) or decane (NBI-Dec, Scheme 2B). The *p*(NB-Hep) and *p*(NBI-Hep) polymer series are similar in chemical composition to each of the two different BBCP backbones, allowing comparison into the BBCP backbone dynamics without the influence of polymeric side-chains. Additionally, the *p*(NBI-Dec) series is similar to the *p*(NBI-Hep) series and the omission of the carbonyl group on the *p*(NBI-Dec) series can isolate the impact of the carbonyl group versus the impact from the norbornene imide group.

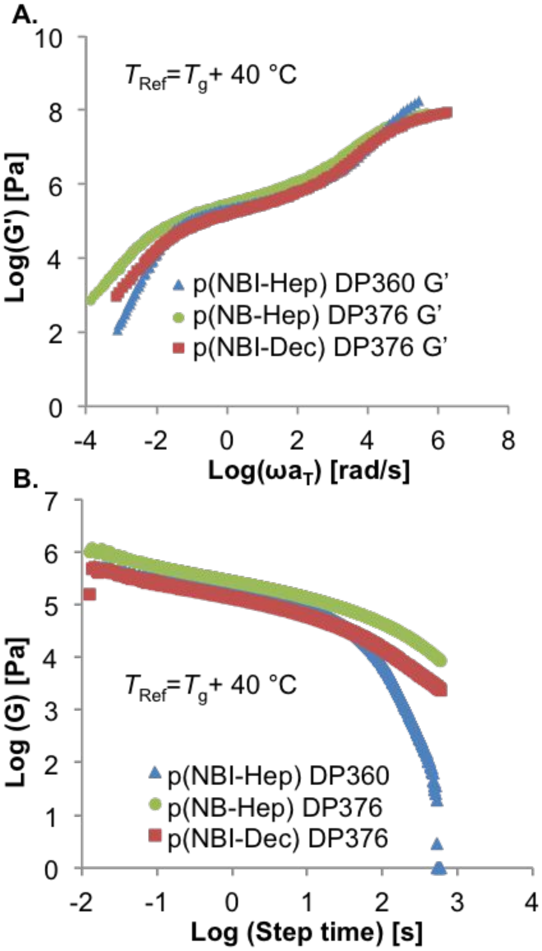

Figure 5. Storage modulus mastercurves of each of the three linear homopolymers at comparable DP (A.) and 5% step-strain stress relaxation tests of each of the linear homopolymers (B.) at a $T_{\mathrm{Ref}} = T_{\mathrm{g}} + 40$ °C.

The storage modulus mastercurves, covering a range of 8 to 10 orders of magnitude in frequency, constructed via standard time and temperature superposition (TTS) processes at a reference temperature $T_{\mathrm{Ref}} = T_{\mathrm{g}} + 40$ °C for each of the three linear polymers at similar DP is shown in Figure 5A. All three polymers displayed characteristic regions similar to those of conventional linear polymers: a glass-to-rubber transition region at high frequency, a rubbery plateau, and a terminal flow region at low frequency. These mastercurves highlight the differences in the polymer dynamics that can be attributed to the backbone. The most significant difference between each of the polymers can be seen in the chain relaxation time (τ_1). The chain relaxation time marks the onset of the terminal flow regime and can be estimated at the crossover frequency (G' (ω) = G" (ω)).[47] Specifically, the τ_1 was estimated to be 116 s for *p*(NB-Hep) DP376, 26 s for *p*(NBI-Hep) DP360, and 41 s for *p*(NBI-Dec) DP376. The faster τ_1 of *p*(NBI-Hep) compared to the τ_1 of *p*(NBI-Dec) can be attributed to a much faster segmental relaxation process, which sets the monomer friction coefficient that governs the chain relaxation process.[48] However, the reduction of τ_1 from *p*(NB-Hep) to *p*(NBI-Hep) at isofrictional conditions can be related to the degree of chain entanglement and the rubbery elasticity, which can be estimated by a comparison of the values of both phase angle minimums shown in the van Gurp-Palmen (VGP) plots shown in Figure 6 and the magnitude of the plateau modulus (G_N^0) in the mastercurve for *p*(NB-Hep) and *p*(NBI-Hep) (Figure 5A).[49,50] The magnitude of G_N^0 can be reliably estimated from the local minimum in the VGP plots shown in Figure 6.[51] Accordingly, the minimum phase angle and G_N^0 value for the *p*(NB-Hep) DP376 were determined to be 26° and 2.40 x 10^3 Pa, respectively. The minimum phase angle and G_N^0 value for the *p*(NBI-Hep) DP360 were determined to be 26° and 1.89 x 10^3 Pa, respectively. The rubbery elasticity of the *p*(NB-Hep) DP376 sample is higher in magnitude than that of the *p*(NBI-Hep) DP360 sample, which follows the fact that the less elastic material has a reduced τ_1. To confirm the trend seen in the estimated τ_1 values from the mastercurves, a 5% step-strain stress relaxation experiment was conducted on each polymer sample at $T_{\mathrm{Ref}} = T_g + 40$ °C. Indeed, the same trend appears over a time-span of 10 minutes (Figure 5B). The *p*(NBI-Hep) DP360 sample relaxes back to 0 Pa within the time frame, while the *p*(NBI-Dec) DP376 relaxes to approximately 2,405 Pa and the *p*(NB-Hep) DP376 sample relaxes to approximately 8,557 Pa.

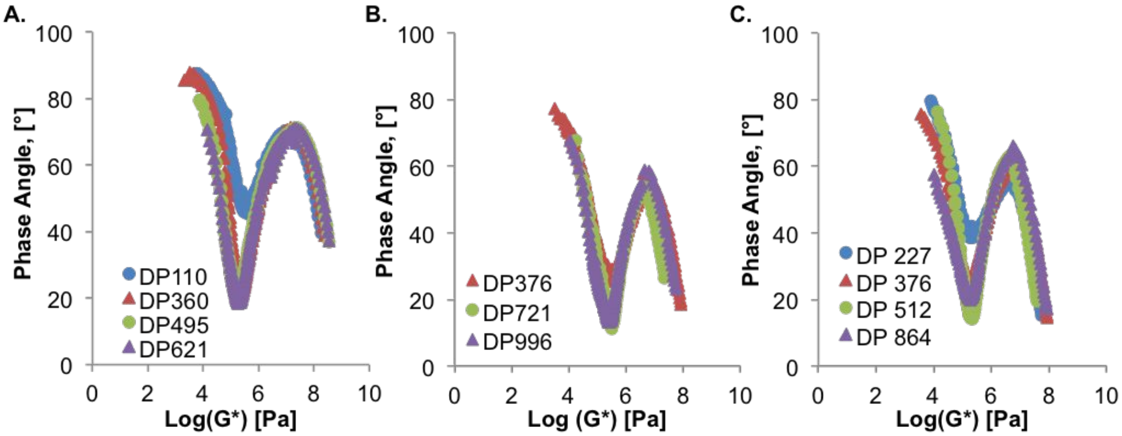

Figure 6. Van Gurp-Palmen plots at isofrictional conditions of $T_{\mathrm{Ref}} = T_g + 40$ °C for the p(NBI-Hep) series (A), the p(NB-Hep) series (B), and the p(NBI-Dec) series (C).

Additionally, by analyzing the temperature dependence of the shift factors (a_T) used in the TTS of the mastercurves for each of the linear polymers as described by the Williams-Landel-Ferry (WLF) equation, it is possible to obtain a fragility index value (m_f) for each of the three polymer series (Figure S117). [52,53] The m_f value describes the temperature dependence of the relaxation processes of the polymer near its T_g value (p(NBI-Hep) T_g = 38 °C, p(NB-Hep) T_g = - 44 °C, p(NBI-Dec) T_g = 57 °C). [54,55,56] The higher the m_f value, the more drastic the temperature dependence and the more fragile the polymer. The m_f values of the *p*(NB-Hep) series, the *p*(NBI-Hep) series, and the *p*(NBI-Dec) series are 42.6, 77.8, and 64.5, correspondingly. The significant difference between the *p*(NB-Hep) series and the *p*(NBI-Hep) series demonstrates the difference in temperature dependence of the polymer relaxation close to the T_g as a result of the backbone composition. Also, the fact that the *p*(NBI-Hep) series has a higher m_f value implies that it experiences greater steric repulsions among monomer segments[57] than that of the *p*(NB-Hep) series which likely contributes to the lower magnitude of rubbery elasticity observed in the G_N^0values (Figure 5A). The stiffer, more rod-like character of the *p*(NBI-Hep) series compared to the *p*(NB-Hep) series can also be seen in solution when comparing the z-average radius of gyration to the M_n of each series in tetrahydrofuran (THF) (Figure S21). Furthermore, the carbonyl group on the *p*(NBI-Hep) series significantly increases the fragility of the polymer compared to that of the *p*(NBI-Dec) series.

Conversely, the polymer dynamics at isofrictional conditions and similar DP of the four homobrush polymers (*p*(NB-PLA), *p*(NBI-PLA), *p*(NB-PS), and *p*(NBI-PS)) exhibit a faster τ_1 with backbones composed of the norbornene group and a slower τ_1 with backbones composed of the norbornene imide group within polymers containing the same side-chain composition (Figure 7A and 7B). Again, these storage modulus mastercurves, covering a window of 8 to 10 orders of magnitude in frequency, were constructed via standard TTS processes at a reference temperature $T_{Ref} = T_g + 30$ °C for each of the four homobrush polymers. As brush polymers do not exhibit crossover points between the storage and loss modulus, the point at which the storage and loss modulus mastercurves begin transitioning into the terminal regime at low frequencies was used to estimate the τ_1 values for the homobrush polymers. The estimated τ_1 for *p*(NB-PLA) DP159, *p*(NBI-PLA) DP189, *p*(NB-PS) DP172, and *p*(NBI-PS) DP140 is 4 s, 12 s, 43 s and 67 s, respectively. This trend can once again be confirmed by the results of the 5 %

step-strain stress relaxation test where p(NB-PLA) DP159 relaxes to 0 Pa while p(NBI-PLA) DP189 relaxes to 10 Pa and p(NB-PS) DP172 relaxes to 272 Pa while p(NBI-PS) DP140 relaxes to 895 Pa (Figure 7C and 7D).

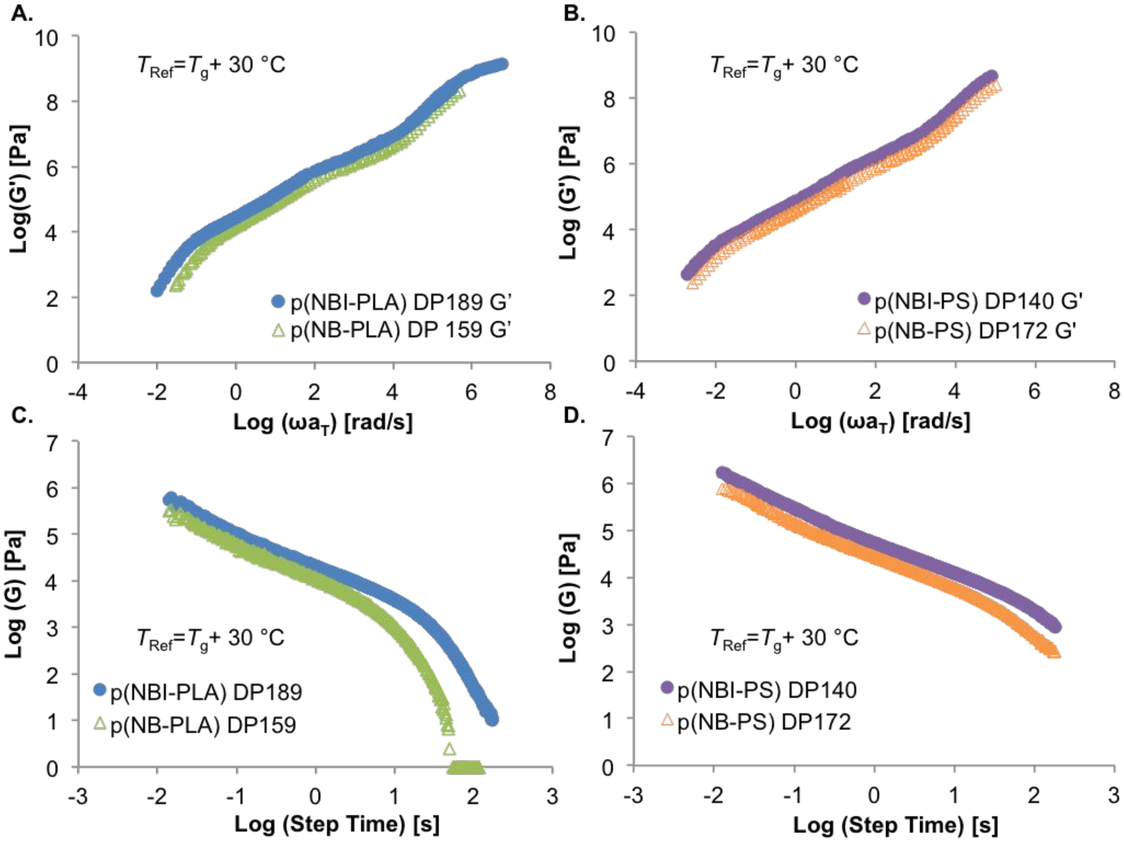

Figure 7. Storage modulus mastercurves of *p*(NB-PLA) and *p*(NBI-PLA) homobrush polymers (A.) and of *p*(NB-PS) and *p*(NBI-PS) homobrush polymers (B.) at a $T_{\mathrm{Ref}} = T_g + 30$ °C. 5% step-strain stress relaxation tests of each of the 2 PLA homobrush polymers (C.) and each of the 2 PS homobrush polymers (D.) at a $T_{\mathrm{Ref}} = T_g + 30$ °C.

Although it may seem that this observed trend for brush homopolymer τ_1 values is in direct contrast with what was observed in the linear homopolymer case (Figure 5), the slower τ_1 for the NBI backbone, once it is incorporated into a brush polymer architecture, confirms the findings that the polymers constructed from NBI monomers yields a more fragile, and likely stiffer, backbone than the polymer constructed from NB monomers. This observation may be attributed to the concept of excluded volume and its effect on brush polymers.36 The *p*(NB-PLA) or the *p*(NB-PS) brushes have a greater amount of excluded volume based on the degrees of freedom that the backbone composition affords the side chains closer to the backbone compared to that afforded to the side chains by the *p*(NBI-PLA) or the *p*(NBI-PS) brushes. This additional excluded volume translates into a more rigid brush macromolecule, which would manifest into a faster τ_1 for the homobrush in the same way that a more fragile linear polymer would relax faster than a stronger linear polymer.

Once again, however, this insight into the relaxation of the homobrush polymers in the present study appears to contradict the differences observed in the abilities of the *p*(NB-PLA)-*b*-*p*(NB-PS) BBCP versus the *p*(NBI-PLA)-*b*-*p*(NBI-PS) BBCP to self-assemble to photonic crystals capable of reflecting longer wavelengths of light as seen in Figures 1 and 2. To resolve this apparent contradiction, it is important to consider the two distinct relaxation processes associated with lamellae forming BBCP that are not present in the relaxation of homobrush polymers.44 At shorter time scales, the relaxation of BBCPs with unentangled and densely grafted side chains is attributed to the cooperative mobility of internal slip layers within microphase-separated domains. This slipping is due to a high concentration of free chain ends in the middle of each domain. However, it was observed that the microphase separation dominates the longer time scale relaxation. The nanostructure morphology and the interface between the two microphase-separated domains are relatively soft, and therefore, require longer times to relax stress.

Consequently, by applying this dual mode relaxation concept to the present study, it can be suggested that the more fragile backbone composition of the norbornene imide group and inherently less amount of excluded volume of the side-chains attached to the norbornene imide backbone both combine to produce a more efficient interfacial relaxation process and a more locally ordered morphology for the *p*(NBI-PLA)-*b*-*p*(NBI-PS) BBCP as compared to the *p*(NB-PLA)-*b*-*p*(NB-PS) BBCP. With more efficient interfacial relaxation, the regions of local ordering will be more prevalent and less energy input will be required for the domains to fully microphase segregate. Additionally, the more fragile backbone allows for higher DP to increase the domain size in a more direct manner.

CONCLUSIONS

Four MW series of well-defined brush block copolymers with near identical side chain compositions but varying backbone compositions were synthesized using ruthenium-mediated ROMP. These BBCP materials were then thermally annealed to promote self-assembly into a periodic dielectric nanostructure able to interact with and reflect wavelengths of light throughout the UV and visible spectrum. Comparisons between the resulting reflections and nanostructure morphology of the polymeric photonic crystals with different backbone compositions lead to some significant observations and suggestions. The backbone composition dramatically affects the ability of the BBCP material to efficiently self-assemble into a lamellar nanostructure with regions of locally ordered domains large enough to reflect light across the visible spectrum from blue to red.

To gain further insight into the differences in the ability of brushes with different backbone compositions to self-assemble in the melt state, a series of linear and brush homopolymers were synthesized using ruthenium-mediated ROMP. These homopolymers mimicked the backbone composition of the BBCP materials and allowed for isolating and examining the polymer dynamics of the backbone without side-chains attached through a rheological study. By analyzing the observed τ_1 values, G_N^0values, and fragility values of the linear polymers, the norbornene imide backbone composition was determined to be inherently less elastic and more fragile than the norbornene backbone composition. Furthermore, from the rheological analysis of the homobrush polymers of each of the block and backbone compositions present in the BBCP materials, it is clear that the backbone composition significantly affected the dynamics of each homobrush in a similar way. The nature of the backbone's effect stems from the concept of excluded volume,36 which allows the norbornene backbone composition to result in a stiffer brush macromolecule. However, when considering the present observations in the self-assembly of BBCPs with different backbone compositions and the observation of dual power law relaxations for lamellae forming BBCPs,44 it can be suggested that an more fragile backbone is necessary in part to reduce the interfacial relaxation process to promote large regions of local ordering within the photonic crystal film, as well as be able to efficiently reflect beyond blue wavelengths of light by increasing the DP of each block. Therefore, the findings of this study present the brush backbone structure as another important characteristic to consider when using ROMP to synthesize macromolecules with tailored properties.

EXPERIMENTAL METHODS

$(H_2IMes)(PPh_3)(Cl)_2RuCHPh$ was purchased from Umicore and was converted to $(H_2IMes)(py)_2(Cl)_2RuCHPh$ via literature procedure.[58] All other chemicals were purchased from Sigma-Aldrich or VWR. All polymerizations were performed in a nitrogen-filled glovebox unless stated otherwise. Column chromatography was performed using a Combiflash Rf+ autocolumn from Teledyne ISCO. NMR spectra were recorded on a Bruker Ultrashield 400 MHz spectrometer. Chemical shifts were referenced using internal solvent resonance, ^1H: 7.26 ppm and ^{13}C: 77.16 ppm for $CDCl_3$. The chemical shifts are reported as parts per million relative to tetramethylsilane. Deuterated chloroform was purchased from Cambridge Isotope Laboratories.

Analysis of isolated and vacuum-dried polymer MW and dispersity was performed using gel permeation chromatography (GPC) coupled with multi-angle light scattering (MALS), using an Agilent HPLC fitted with one guard column and three Plgel 5 uM MIXED-C gel permeation columns in series. The detectors used were a Wyatt Technology TrEX differential refractometer and a Wyatt Technology miniDAWN TREOS light scattering detector, which allows the direct measurement of absolute MW. Absolute MWs were determined using dn/dc values calculated by assuming 100% mass recovery of the polymer sample injection into the GPC. The solvent used was tetrahydrofuran (THF) with a flow rate of 1.0 mL per minute. The R_z value of each polymer was calculated using the multi angle light scattering detector in the miniDAWN TREOS.

Thermal Gravimetric Analysis (TGA) was conducted using a TA Instruments TGA Q50 or TGA Q500. The thermal decomposition data was obtained under a nitrogen gas flow of 40 mL/min by ramping the temperature from 25 °C up to 850 °C at a ramp rate of 10 °C/minute.

Differential Scanning Calorimetry (DSC) was conducted using a TA Instruments DSC 2500. To erase thermal history, an initial sweep ramped from 0 °C to 200 °C at a ramp rate of 10 °C/min. The temperature was held constant at 200 °C for 3 minutes before it was cooled to 0 °C at a ramp rate of -10 °C/min where the temperature was held constant at 0°C for 3 minutes. Thermal data was collected from the second sweep which consists of ramping the temperature from 0 °C up to 200 °C at a rate of 5 °C/min. However, for the NB-Hep polymer, the range of the test was -90 °C to 150 °C, but the rates of heating and cooling were the same as the rates used to test the rest of the polymers. This analysis was performed to measure the low glass transition temperature of that particular polymer.

The rheological experiments were performed using a DHR-2 rheometer (TA Instruments) with 8 mm parallel plate geometry under nitrogen purge. The sample was loaded onto the 8 mm plate at experimental conditions until melting and then slowly pressed until the gap was approximately 1 mm using axial stress. Before testing, the samples were kept for 30 minutes – 2 hours until the axial stress was 0.0 ± 0.2 N. First, strain sweep experiments were performed to determine the linear viscoelastic region of the materials. Oscillatory frequency sweep was carried out from 0.01 to 100 rad/s with a strain in the linear strain regime. The temperature regime for the reference temperature of the time-temperature superposition (TTS) was determined based on the T_g of the polymer series. The TTS was completed with a vertical and lateral shift within the TA Trios Software. Van Gurp-Palmen plots were used to establish the validity of the time-temperature superposition of the polymer series.

Reflection measurements were performed using a Cary 5000 UV/vis/NIR spectrophotometer, equipped with an integrating sphere diffuse reflectance accessory (DRA) (Internal DRA-2500) using the standard wide-open aperture. The samples were scanned at a rate of 600 nm/min from 800 to 280 nm.

Scanning electron microscopy images were taken on a JEOL JSM-6500F field emission scanning electron microscope after freeze fracturing the films and then staining the fractured films with RuO_4. The samples were coated with a 10 nm thick layer of gold before imaging.

Small-Angle X-ray Scattering (SAXS) characterization was carried out at the beamline 12-ID-B of the Advanced Photon Source (APS) at Argonne National Laboratory. X-rays of wavelength 0.9322 Å (13.3 keV) were used, and the sample to detector distance was calibrated using silver behenate as a standard. Samples were mounted on an XY stage with thermal capabilities. Each sample was exposed to the X-ray beam for 1s. The scattered X-rays were collected with a Pilatus2M detector located about 2 m downstream from the sample position. The 1D scattering spectra were obtained by radially averaging the images into scattering intensities versus the scattering vector, q.

A more detailed and thorough experimental method can be found in the Supporting Information document.

CONFLICTS OF INTEREST

The authors declare no competing financial interests.

ACKNOWLEDGEMENTS

B.M.B. and G.M.M. would like to thank the Colorado State University, the National Science Foundation (CMMI- 1634941), and the National Institute of General Medical Sciences of the National Institutes of Health under Award Number R35GM119702. The content is solely the responsibility of the authors and does not necessarily represent the official views of the National Institutes of Health. This research used beamline 12-ID-B of the Advanced Photon Source (APS) at Argonne National Laboratory, a U.S. Department of Energy (DOE) Office of Science User Facility operated for the DOE Office of Science by Argonne National Laboratory under Contract No. DE-AC02-06CH11357. Thank you to T.Bailey's research group at CSU, especially A. Klug, for their beamtime generosity and their coordination efforts in making the trip to ANL. The authors would also like to sincerely thank Y. Ding, J. Cole, R. Pearson, and B. McCarthy for insightful discussions, as well as, M. Kudisch for his photography expertise and time.

REFERENCES

---

1. E. Yablonovitch, *Sci. Am.* **2001**, *285*, 46-55.

2. J. D. Joannopoulos, S. G. Johnson, J. N. Winn, R. D. Meade, *Photonic Crystals: Molding the Flow of Light,* 2nd Ed.; Princeton University Press: Princeton, NJ, **2008**.

3. A. F. Abouraddy, M. Bayindir, G. Benoit, S. D. Hart, K. Kuriki, N. Orf, O. Shapira, F. Sorin, B. Temelkuran, Y. Fink, *Nat. Mater.* **2007**, *6*, 336-347.

4. F. Sorin, A. F. Abouraddy, N. Orf, O. Shapira, J. Viens, J. Arnold, J. D. Joannopoulus, Y. Fink, *Adv. Mater.* **2007**,*19,* 3872-3877.

5. W. J. Schrenk, R. A. Lewis, J. A. Wheatley, C. B. Arends, *Int. Polym. Process* **1991**, *6*, 255-256

6. B. M. Boyle, T. A. French, R. M. Pearson, B. G. McCarthy, G. M. Miyake, *ACS Nano* **2017**, *11*, 3052-3058.

7. F. S. Bates, M. A. Hillmyer, T. P. Lodge, C. M. Bates, K. T. Delaney, G. H. Fredrickson, *Science* **2012**, *336,* 434-440.

8. A. C. Edrington, A. M. Urbas, A. C. DeRege, C. X. Chen, T. M. Swager, N. Hadjichristidis, M. Xenidou, L. J. Fetters, J. D. Joannopoulos, Y. Fink, E. L. Thomas, *Adv. Mater.* **2001**, *13,* 421-425.

9. Y. Fink, A. M. Urbas, M. G. Bawendi, J. D. Joannopoulos, E. L. Thomas, *J. Lightwave Technol.* **1999**, *17,* 1963-1969.

10. J.F. Galisteo-López, M. Ibisate, R. Sapienza, L. S. Froufe-Pérez, Á. Blanco, C. López, *Adv. Mater.* **2011**, *23*, 30-69.

11. B. B. Patel, D. J. Walsh, D. H. Kim, J. Kwok, B. Lee, D. Guironnet, Y. Diao *Sci. Adv.* **2020,** *6*, eaaz7202

12. M. Appold, E. Grune, H. Frey, M. Gallei, *ACS Appl. Mater. Interfaces* **2018**, *10,* 18202-18212.

13. V. A. Piunova, G. M. Miyake, C. S. Daeffler, R. A. Weitekamp, R. H. Grubbs, *J. Am. Chem. Soc.* **2013**, *135*, 15609-15616.

---

14. B. R. Sveinbjornsson, R. A. Weitekamp, G. M. Miyake, Y. Xia, H. A. Atwater, R. H. Grubbs, *Proc. Natl. Acad. Sci. U. S. A.* **2012**, *109,* 14332-14336.

15. A. B. Chang, C. M. Bates, B. Lee, C. M. Garland, S. C. Jones, R. K. W. Spencer, M. W. Matsen, R. H. Grubbs, *Proc. Natl. Acad. Sci. U. S. A.* **2017**, *114*, 6462-6467.

16. F. S. Bates, G. H. Fredrickson, *Phys. Today* **1999**, *52*, 32-38

17. C. M. Bates, F. S. Bates, *Macromolecules* **2017,** *50*, 3- 22

18. P. D. Hustad, G. R. Marchand, E. I. Garcia-Meitin, P. L. Roberts, J. D. Weinhold, *Macromolecules* **2009**, *42*, 3788-3794.

19. B. M. Boyle, O. Heinz, G. M. Miyake, Y. Ding, *Macromolecules* **2019**, *52*, 3426-3434.

20. Z. Qian, Y. P. Koh, R. P. Madhusudhan, A. B. Chang, T. –P. Lin, P. E. Guzmán, R. H. Grubbs, S. L. Simon, G. B. McKenna, *Macromolecules* **2019**, *52*, 2063-2074

21. F. Dutertre, K. –T. Bang, E. Vereroudakis, B. Loppinet, S. Yang, S. –Y. Kang, G. Fytas, T. –L. Choi, *Macromolecules* **2019**, *52*, 3342-3350

22. G. M. Miyake, R. A. Weitekamp, V. A. Piunova, R. H. Grubbs, *J. Am. Chem. Soc.* **2012**, *134*, 14249-14254

23. Y. Xia, B. D. Olsen, J. A. Kornfield, R. H. Grubbs, *J. Am. Chem. Soc.* **2009**, *131*, 18525-18532

24. G. M. Miyake, V. A. Piunova, R. A. Weitekamp, R. H. Grubbs, *Angew. Chem. Int. Ed.* **2012**, *51*, 11246-11248

25. R. J. Macfarlane, B. Kim, B. Lee, R. A. Weitekamp, C. M. Bates, F. L. Siu, A. B. Chang, K. T. Delaney, G. H. Fredrickson, H. A. Atwater, R. H. Grubbs, *J. Am. Chem. Soc.* **2014**, *136*, 17374-17377

26. R. Verduzco, X. Li, S. L. Pesek, G. E. Stein, *Chem. Soc. Rev.* **2015**, *44*,2405.

27. S. J. Dalsin, T. G. Rions-Maehren, M. D. Beam, F. S. Bates, M. A. Hillmyer, M. W. Matsen, *ACS Nano* **2015**, *9,* 12233-12245.

28. W. Gu, J. Huh, S. W. Hong, B. R. Sveinbjornsson, C. Park, R. H. Grubbs, T. P. Russell, *ACS Nano* **2013**, *7,* 2551-2558.

29. W. F. M. Daniel, J. Burdynska, M. Vatankhah-Varnoosfaderani, K. Matyjaszewski, J. Paturej, M. Rubinstein, A. V. Dobrynin, S. S. Sheiko, *Nat. Mater.* **2016**, *15*, 183-190.

---

30. S. J. Dalsin, M. A. Hillmyer, F. S. Bates, *Macromolecules* **2015**, *48,* 4680-4691.

31. M. Hu, Y. Xia, G. B. McKenna, J. A. Kornfield, R. H. Grubbs, *Macromolecules* **2015**, *44,* 6935-6943.

32. I. N. Haugan, M. J. Maher, A. B. Chang, T. –P. Lin, R. H. Grubbs, H. A. Hillmyer, F. S. Bates, *ACS Macro Lett.* **2018**, *7*, 525-530.

33. S. Rathgeber, T. Pakula, A. Wilk, K. Matyjaszewski, K. L. Beers, *J. Chem. Phys.* **2005,** *122*, 124904.

34. S. Dutta, M. A. Wade, D. J. Walsh, D. Guironnet, S. A. Rogers, C. E. Sing, *Soft Matter* **2019**, *15,* 2928.

35. J. Paturej, T. Kreer, *Soft Matter* **2017**, *13*, 8534.

36. Y. Saito, M. Kikuchi, Y. Jinbo, A. Narumi, S. Kawaguchi, *Macromolecules* **2015**, *48*, 8971-8979.

37. Y. Saito, L. T. N. Lien, Y. Jinbo, J. Kumaki, A. Narumi, S. Kawaguchi, *Polym. J.* **2013**, *45*, 193-201.

38. H. Iwawaki, O. Urakawa, T. Inoue, Y. Nakamura, *Macromolecules* **2012,** *45,* 4801-4808.

39. Y. Nakamura, T. Norisuye, *Polym. J.* **2001**, *33*, 874 – 878.

40. S. S. Sheiko, B. S. Sumerlin, K. Matyjaszewski, *Prog. Polym. Sci.* **2008**, *33*, 759-785.

41. J. Rzayev, *ACS Macro Lett.* **2012**, *1*, 1146-1149

42. D. J. Walsh, S. Dutta, C. E. Sing, D. Guironnet, *Macromolecules* **2019**, *52*, 4847-4857.

43. S. C. Radzinski, J. C. Foster, R. C. Jr. Chapleski, D. Troya, J. B. Matson, *J. Am. Chem. Soc.* **2016**, *138,* 6998-7004.

44. B. M. Yavitt, H. –F. Fei, G. N. Kopanati, H. H. Winter, J. J. Watkins, *Macromolecules* **2019**, *52*, 1557-1566

45. H. –F. Fei, B. M. Yavitt, X. Hu, G. Kopanati, A. Ribbe, J. J. Watkins, *Macromolecules* **2019**, *52*, 6449-6457

---

46. Y. Gai, S. Dong-Po, B. M. Yavitt, J. J. Watkins, *Macromolecules* **2017,** *50,* 1503-1511.

47. P. Sunthar, In *Rheology of Complex Fluids*; A. P. Deshpande, J. M. Krishnan, S. Kumar, Eds.; Springer: New York, 2010.

48. A. Kisliuk, Y. Ding, J. Hwang, J. S. Lee, B. K. Annis, M. D. Foster, A. P. Sokolov, *J. Polym. Sci., Part B: Polym. Phys.* **2002**, *40*, 2431-2439

49. M. van Gurp, J. Palmen, *Rheol. Bull.* **1998**, *67*, 5-8

50. S. Trinkle, C. Friedrich, *Rheol. Acta* **2001**, *40*, 322-328

51. K. L. Ngai, M. Paluch, *J. Chem. Phys.* **2004**, *120*, 857

52. M. L. Williams, R. F. Landel, J. D. Ferry, *J. Am. Chem. Soc.* **1955**, *77*, 3701-3707

53. J. D. Ferry, In *Viscoelastic Properties of Polymers,* 3rd Ed.; John Wiley & Sons: New York, 1980; p 304

54. Y. Ding, A. P. Sokolov, *Macromolecules* **2006**, *39*, 3322-3326

55.K. Kunal, C. G. Robertson, S. Pawlus, S. F. Hahn, A. P. Sokolov, *Macromolecules* **2008**, *41,* 7232-7238

56. K. L. Ngai, C. M. Roland, *Macromolecules* **1993**, *26*, 6824-6830

57. S. Ciarella, R. A. Biezemans, L. M. C. Janssen *Proc. Natl. Acad. Sci. U. S. A.* **2019,** *116*, 25014 – 25022.

58. J. A. Love, J. P. Morgan, T. M. Trnka, R. H. Grubbs *Angew. Chem., Int. Ed.* **2002**, *41*, 4035-4037.

GRAPHICAL ABSTRACT for

Impact of Backbone Composition on Homopolymer Dynamics and Brush Block Copolymer Self-Assembly

Bret M. Boyle,[a] Joseph L. Collins,[a] Tara E. Mensch,[a] Matthew D. Ryan,[a] Brian S. Newell,[a] and Garret M. Miyake[a]*

[a]Department of Chemistry,
Colorado State University, Fort Collins, Colorado
*Corresponding Authors: Garret.Miyake@colostate.edu